Andean Geology 48 (3): 496-513. September, 2021
doi: 10.5027/andgeoV48n3-3327

Andean Geology
www.andeangeology.cl

Diffuse gases in soil of Araró-Simirao geothermal system, Michoacán, Mexico

***Isabel Pérez-Martínez[1], Ruth Esther Villanueva-Estrada[2], Augusto Rodríguez-Díaz[3], Carles Canet[3, 4], Rocío García[4], José Alfredo Ramos-Leal[5], Donají García[4], Jaziel Froylan Cambrón[4]**

[1] *CONACYT- Geophysics Institute, UNAM. Circuito de la Investigación Científica s/n Ciudad Universitaria, Alcaldía Coyoacán, 04510 Ciudad de México, México.*
perezm@igeofisica.unam.mx

[2] *Geophysics Institute, Michoacán Unit, UNAM. Km 8 Antigua carretera a Pátzcuaro 8701, Col. Ex Hacienda de San José de la Huerta, 58190 Morelia, Michoacán.*
ruth@geofisica.unam.mx

[3] *Geophysics Institute, UNAM. Circuito de la Investigación Científica s/n Ciudad Universitaria, Alcaldía Coyoacán, 04510 Ciudad de México, México.*
augusto@geofisica.unam.mx; ccanet@atmosfera.unam.mx

[4] *Atmosphere Science Center, UNAM. Circuito de la Investigación Científica s/n Ciudad Universitaria, Alcaldía Coyoacán, 04510 Ciudad de México, México.*
gmrocio@atmosfera.unam.mx; donaji.ga@gmail.com; jazfro.geokm9@gmail.com

[5] *Applied Geosciences Division, Potosin Institute of Scientific and Technological Research, (IPICYT), Camino a la Presa San José 2055, Lomas 4a Sección, 78216 San Luis Potosí, San Lui Potosí.*
jalfredo@ipicyt.edu.mx

** Corresponding author: perezm@igeofisica.unam.mx*

ABSTRACT. The Araró-Simirao geothermal system is located in the southeastern part of the Cuitzeo Lake depression, in the central part of the TransMexican Volcanic Belt (TMVB) province. It is a convective hydrothermal system dominated by sodium chloride water and high boron content. The thermal springs mainly release CO_2 and lower concentrations of H_2S, H_2, and noble gases (He, Ne, and Ar). The aim of this study was to delimit the upflow areas in this geothermal system by determining the relationships between diffuse gas emission concentrations in soils and the zones of the greatest plausible permeability. Three sampling campaigns were carried out in 2018 (August and November) and 2019 (May). In these campaigns, diffuse gas emission in soils (CO_2, Rn, and Hg vapors) and soil temperature were measured. The diffuse gas emission measurements ranged from 0.8 to 1,421 g $m^{-2}d^{-1}$ for CO_2 flux, from 0.49 to 2,914 ng/m^3 for gaseous elemental mercury (GEM), from 1,060 to 124,100 Bq/m^3 for ^{222}Rn, and from 0 to 7,511 Bq/m^3 for ^{220}Rn. The highest values were obtained in the dry season (May). Several anomalous zones of CO_2 fluxes, GEM, and ^{222}Rn were found to match faults and lineaments, interpreted as the greatest permeability zones. The zone with the highest values of these three parameters was located in the so-called mud pool at the crossing of the Araró-Simirao fault with a NW-SE (south zone) lineament, which is associated with the upflow zone of the system. Other anomalous zones were located in fracture and/or lineament zones in the central and northern parts of the system, which are associated with the outflow zone. According to the data obtained herein, CO_2 could work as a carrier of Hg and ^{222}Rn in the upflow zone; and this gas may be dissolved in the groundwater in the outflow zone.

Keyword: Diffuse soil emissions, Carbon dioxide flux, Gaseous Elemental Mercury, Radon, Thoron, High permeability zones.

RESUMEN. Gases difusos en suelos del sistema geotérmico de Araró-Simirao, Michoacán, México. El sistema geotérmico Araró-Simirao está ubicado en el sector sureste de la depresión del lago Cuitzeo, en la parte central de la provincia del Cinturón Volcánico TransMexicano (TMVB). Es un sistema hidrotermal convectivo, líquido dominante, con agua tipo clorurada-sódica y alto contenido de boro. Los manantiales termales emiten principalmente gases de CO_2 y cantidades menores de H_2S, H_2 y gases nobles (He, Ne y Ar). El objetivo de este estudio fue delimitar las áreas

de ascenso de fluidos en el sistema geotérmico, determinando la relación entre las áreas con mayores flujos de gases difusos en los suelos y las zonas de mayor permeabilidad. Se realizaron tres campañas de muestreo en 2018 (agosto y noviembre) y 2019 (mayo). En estas campañas se realizaron mediciones de emisiones difusas de gases (CO_2, Rn y vapores de Hg) y de la temperatura del suelo. Las concentraciones obtenidas para la emisión de gases difusos fueron: de 0,8 a 1.421 g $m^{-2}d^{-1}$ para el flujo de CO_2, de 0,49 a 2.914 ng/m^3 para el mercurio elemental gaseoso (GEM), de 1.060 a 124.100 Bq/m^3 para ^{222}Rn y de 0 a 7.511 Bq/m^3 para ^{220}Rn. Los valores más altos se registraron en la época seca (mayo). Se determinó que varias zonas con flujos anómalos de CO_2, GEM y ^{222}Rn coincidían con zonas de fallas y lineamientos, interpretados como las de mayor permeabilidad. La zona con los valores más altos de estos tres parámetros se ubicó en la denominada poza de lodo, en el cruce de la falla Araró-Simirao con un lineamiento NW-SE (zona sur), el cual está asociado a la zona de *upflow* del sistema (ascenso vertical de gases). Otras anomalías se ubicaron en zonas de fracturas y/o lineamientos en la parte central y norte del sistema, las cuales están asociadas con la zona de *outflow*. De acuerdo con los resultados obtenidos, el CO_2 podría actuar como portador de los gases de Hg y ^{222}Rn en la zona de *upflow*; mientras que, en la zona de *outflow*, este gas podría estar presente en forma disuelta en el agua subterránea.

Palabras clave:Emisiones difusas del suelo, Flujo de dióxido de carbono, Mercurio elemental gaseoso, Radón, Torón, Zonas de alta permeabilidad.

1. Introduction

Innovative, cutting-edge techniques to improve geochemical exploration of geothermal systems are currently under development. These techniques are based on the measurement of diffuse gas emissions (*e.g.,* Hg, CO_2, H_2S, Rn, and He) in soils to find anomalies that can be used as geothermal resources exploration tools (Owens, 2013). The study of diffuse gas emissions in soils has helped to define the limits of geothermal systems, delineate preferential flow zones of greater permeability as fault zones, and better understand water-rock interaction processes (Murray, 1997; Fridriksson, 2009; Jennejohn, 2009; Owens, 2013; Hernández *et al.,* 2015). These techniques involve placing detectors in the ground, and the resulting measurements represent geochemical signals from the deeper layers. These signals provide evidence for changes that occur in geological systems, such as volcanic activity, the presence of faults, fracture systems, and the trajectories of vertical flows of hot reservoirs (Hernández *et al.,* 2015).

According to Fridriksson (2009), CO_2 measurements (concentration and flux) in released steam allow for the quantification of steam and heat flow. This gas is used as a magma degassing tracer due to its low solubility in silicate melts at moderate pressure, and CO_2 anomalies usually coincide with high-vertical-permeability zones (Mazot *et al.,* 2011; Hernández *et al.,* 2015; Peiffer *et al.,* 2018; Jácome-Paz *et al.,* 2019). According to Padrón *et al.* (2003), high surface concentrations of ^{222}Rn and ^{220}Rn (Thoron) allow for the identification of high-permeability zones and the prediction of flow rates in the same region; thoron, in particular, is associated with high velocity flows due to its short half-life of 5.56 s (Durridge, 2019).

On the other hand, the study of surface vapour mercury anomalies provides information about the existence of hydrothermal circulation patterns. Together with geological data, surface vapour mercury anomalies allow for the limits of the reservoir to be defined and provide a general image of the geometry of the geothermal field (Varekamp and Buseck, 1983). Gaseous elemental mercury (GEM) is associated with active volcanic structures; therefore, surface degassing studies of GEM are often used as tools for the exploration of geothermal resources and for the identification of hydrothermal systems (Bagnato *et al.,* 2009, 2018; Cabassi *et al.,* 2017). The vaporization and emission of Hg under the surface in high-temperature geothermal systems occurs via diffusion through permeable rock regions (Murray, 1997). Hg gas diffusion can be measured upon reaching the surface, while the portion of Hg immobilized by clay and organic material in the soil can be detected by analyzing the material present in the soil surface (Van Kooten, 1987). According to the information presented above, the application of this type of study can provide useful information for the determination of high-permeability areas and types of fluid transport.

The Araró-Simirao geothermal system is located in the southeastern part of the Cuitzeo Lake depression, northeast of the state of Michoacan in the central part of Mexico (Fig. 1A). This geothermal system has been studied since the 1970s (Gutiérrez-Negrín *et al.,* 1989; Viggiano-Guerra and Gutiérrez-Negrín, 2005). According the findings of previous studies, it is a convective system dominated by liquid with sodium chloride waters and high boron content; further, it appears to be a fracture zone reservoir fed by a deep, narrow conduit related to the faults in the area

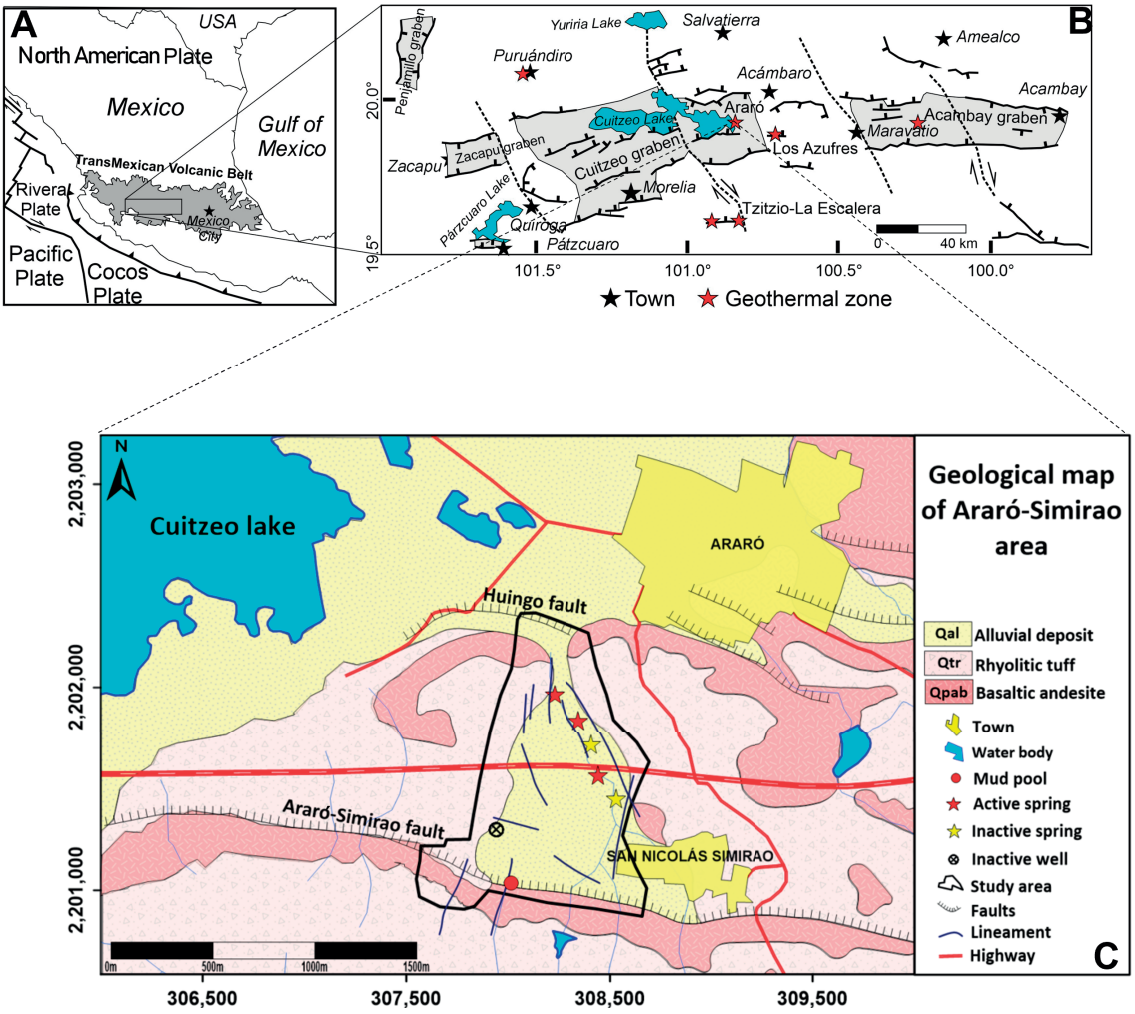

FIG. 1. Localization map of the Araró-Simirao geothermal system. **A.** Current geotectonic configuration of the Mexican territory, in gray the TransMexican Volcanic Belt (TMVB). **B.** Location of the Araró-Simirao area in the central part of the TMVB. **C.** Geological map of the Araró-Simirao area, and the geothermal field. (Modified from: Garduño-Monroy *et al.*, 2009 and Gómez-Tuena *et al.*, 2005. The geological map modified from DETENAL, 1978).

(Viggiano-Guerra and Gutiérrez-Negrín, 2005). The soil type that dominate in the geothermal system area is gleysol, and in the southern part, bordering this system is vertisol (INEGI, 2009). The objective of the present study was to determine the relationships between diffuse gas flow in soils (CO_2, Rn, and GEM) in the areas of the greatest permeability (regional faults) to delimit the vertical ascent areas of fluids in the Araró-Simirao geothermal system. This study provides information regarding the diffuse emissions of gases in soils, which has not been previously reported in this geothermal area.

2. Geologic setting

The Araró geothermal zone is located in a region referred to as the Cuitzeo Lake depression, which is part of a large tectonic graben (with an E-W orientation) that extends from Chapala Lake to Tepetongo (Viggiano-Guerra and Gutiérrez-Negrín, 2003) and is contained within the central sector of the TransMexican Volcanic Belt (TMVB; Israde-Alcántara and Garduño-Monroy, 1999; Ferrari *et al.,* 2012; Gómez-Tuena *et al.,* 2018; Fig. 1B). Three deformation phases have been identified in the Cuitzeo basin: **(1)** a phase in

the mid-late Miocene characterized by left-lateral strike-slip faults with E-W and NE-SW orientations, followed by **(2)** a distensive tectonic phase with a NW-SE orientation that likely started in the Miocene, reactivating the structures of the previous phase, and **(3)** a phase responsible for the formation of several lake basins in areas such as the Chapala and Cuitzeo lakes and the Cuitzeo graben (Garduño-Monroy *et al.,* 1997).

There are three regional systems of normal faults associated with these deformation phases that affect the central part of the TMVB: **(1)** the NNW-SSE system formed by the extension of the Basin and Range, which is dated to the post-Laramide period (<45 Ma), **(2)** the NESW system, which is contemporary to the TMVB, and **(3)** the E-W Morelia-Acambay fault system (MAFS) of the Pleistocene (Garduño-Monroy *et al.,* 2009). The first fault system (NNW-SSE) could be contemporary to the E-W extensional faults and could affect the rock of the Miocene and the Oligocene (Garduño-Monroy, 2019). The MAFS consists of a series of normal E-W and NE-SW faults that cut through the central part of the TMVB and are associated with tectonic lacustrine depressions, such as Chapala, Zacapu, and Cuitzeo (Garduño-Monroy *et al.,* 2009). The tectonic basins are seismically active with large periods of recurrence related to the activity of the MAFS (Mendoza-Ponce *et al.,* 2018). The E-W faults are approximately 7 to 9 Ma old and appeared during the Miocene with evidence of reactivation in paleoseismological records from the Pleistocene and in recent estimates of shallow earthquake hypocenters (<20 km; Mendoza-Ponce *et al.,* 2018). In Cuitzeo, the system has hanging blocks in the northern and southern edges of the lacustrine basin, which form a graben in the western part and a half-graben in the eastern part of the basin (Fig. 1B)

2.1. Lithology and structures

The base-to-roof volcanic stratigraphy of the zone is given by andesites, basaltic andesites, vitreous rhyolites, vitreous fluid rhyolites, rhyolitic tuffs and basalts, and cinder cones. These units are covered by slope deposits and alluvium (Viggiano-Guerra and Gutiérrez-Negrín, 2003). Outcrops in the area can be grouped into three lithological units: **(1)** basaltic andesites of the Early Pleistocene with a slight degree of fracturing that correspond with the escarpments of the Huingo fault (Casarrubias[1] *et al.,* 1990), **(2)** rhyolitic tuffs aged between 1.2 and 9 Ma (Casarrubias[1] *et al.,* 1990; Viggiano-Guerra and Gutiérrez-Negrín, 2003), and **(3)** alluvial deposits (Viggiano-Guerra and Gutiérrez-Negrín, 2005; Fig. 1C).

In the studied area, there are two normal faults (Fig. 2) with a general E-W tendency: the Huingo fault in the north and the Araró-Simirao fault in the south, both of which are apparently active (Viggiano-Guerra and Gutiérrez-Negrín, 2003). These structures form a staggered system toward the NW and are slightly inclined toward the NE. In addition to these principal faults, surface lineaments have been observed (Ávalos, 2016; Vigil, 2017) to preferentially follow an E-W pattern, followed by a NNW-SSE and a NNE-SSW patterns (Fig. 1C).

2.2. Hydrology and hydrothermalism at the Araró-Simirao geothermal system

The Araró-Simirao geothermal system is part of the Cuitzeo Lake hydrographic basin. The aquifer in this region is heterogeneous and anisotropic with semiconfined conditions due to the presence of clay sediments in the area near the lake (CONAGUA, 2018). Where the flow direction is S-N toward the lake. The aquifer also consists of andesitic breccias, basalts, basaltic breccias, and ashes (CONAGUA, 2018). The shallow aquifer in the Araró area consists of clastic fragments and lacustrine sediments with variable thicknesses ranging between 100 and 200 m. The water table can be located at depths ranging from 0 to 25 m (Viggiano-Guerra and Gutiérrez-Negrín, 2003). In the Nicolás Simirao area, the water table is shallow (approximately 1 m deep) and mixed with thermal water. In this area, a clay layer constituted of lacustrine sediments can be inferred to act as an impermeable layer (Viggiano-Guerra and Gutiérrez-Negrín, 2003; CONAGUA, 2018); however, this layer breaks in areas where it is intercepted by faults and fractures, allowing thermalism to manifest and producing superficial deposits of sinter, calcite, and NaCl (Viggiano-Guerra and Gutiérrez-Negrín, 2003).

The surface manifestations of the hydrothermal system consist of sodium chloride hot springs with high boron content, escaping gases, high electrical conductivity (4,600 µS/cm), and a pH between 6 and 8.

[1] Casarrubias, U.; Izunza, G.; Contreras, V. 1990. Estudio geológico de detalle en la zona geotérmica de Araró-Zimirao, Michoacán. CFE Internal Report No. 01-90. Unpublished.

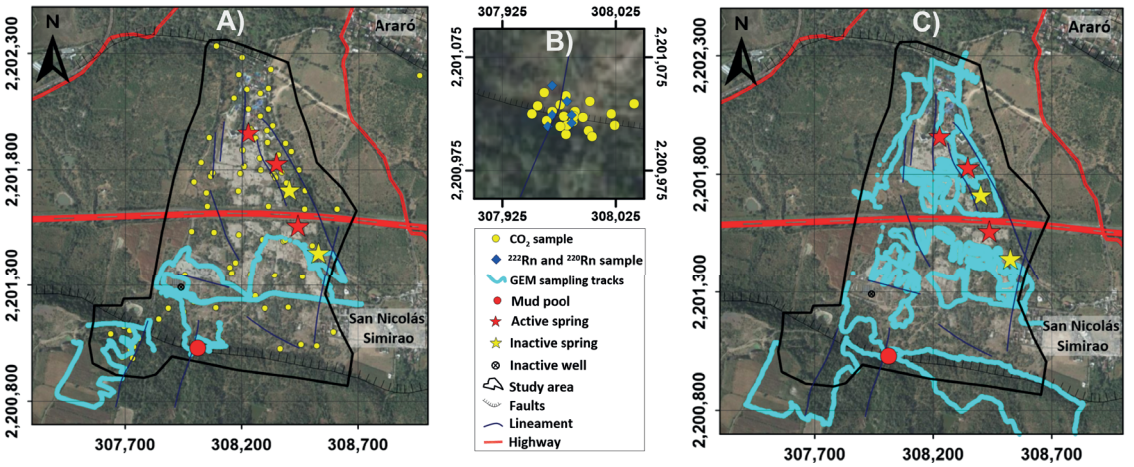

FIG. 2. Location map of diffuse gas sampling points. **A)** Sampling tracks for GEM (August) and diffuse CO_2 Flux (November), both in 2018. **B)** Sampling points for CO_2 Flux, ^{222}Rn and ^{220}Rn, May 2019. **C)** GEM sampling tracks, November 2018.

The temperatures of these manifestations vary from 30 °C to the local boiling point. Geothermometers show temperatures at depths above 200 °C (Viggiano-Guerra and Gutiérrez-Negrín, 2003). The main gases of some springs are CO_2 and, in lower concentrations, H_2S, H_2, and noble gases (He, Ne, and Ar). These characteristics of the water suggest that they come from the mixture of deep geothermal fluids with shallow freshwater aquifers (Viggiano-Guerra and Gutiérrez-Negrín, 2003). This results in rapid discharge with little heat loss where self-sealing processes have occurred, causing the system to deepen (Viggiano-Guerra and Gutiérrez- Negrín, 2003).

3. Methodology

Three sampling campaigns were carried out in the study area during the rainy (August and November) and dry (May) seasons of 2018 and 2019, respectively. In these campaigns, diffuse gas sampling was carried out to measure CO_2, GEM, and ^{222}Rn in the soil, and soil temperatures were measured as well (Fig. 2). To obtain CO_2 flux data, two sampling campaigns were carried out. The first campaign was carried out in November 2018 (the end of the rainy season) from the northern part of the study area near the Huingo and Los Hervideros balnearies to the 15D Atlacomulco-Guadalajara Highway and from the highway to the Araró-Simirao fault trace in the southern part of the study area. Eighty-six CO_2 flux and soil temperature measurements were taken throughout the geothermal system area (Fig. 2A). The other campaign was carried out in May 2019 (the dry season); in this campaign, measurements were taken in specific zones based on the anomalous data obtained from the first sampling campaign as well as data from the zone of interest regarding diffuse gases, such as GEM. Thirty-eight CO_2 flux and soil temperature measurements were taken in this latter campaign (Fig. 2B). Two sampling campaigns were carried out to obtain the GEM concentration data: one in August 2018 and the other in November of the same year. The August route was taken southeast of the town of Araró and south of Highway 15D, which is 8 km in length and occupies approximately 4.2 km^2 in area; 8,385 GEM measurements were taken on this route in total (Fig. 2A). In November, the August tour was repeated with an additional surface in the immediate area of the Huingo and Los Hervideros balnearies. A total area of 6.6 km^2 (length=21.3 km) was covered, resulting in 18,576 GEM measurements (Fig. 2C). To obtain ^{222}Rn concentration data, a sampling campaign was carried out during the dry season (May) of 2019; however, for technical reasons, only six sampling points were obtained. The point distribution was 10 m between each point. The diffuse gas analyses of CO_2, GEM, and ^{222}Rn were carried out using different methods.

3.1. CO_2 measurement method

A West System portable fluxmeter with an A type accumulation chamber was used to measure CO_2. This portable fluxmeter measures CO_2 concentrations

through a non-dispersive infrared spectrometer (NDIR) with a measuring range of 0-20,000 ppm. Readings from this instrument are accurate to 3%. The cumulative chamber is placed on the floor, and concentration variations (ppm) are measured over 90-240 s (West System, 2019). The sampling points were georeferenced using a GPS device, and soil temperatures were recorded using a thermocouple inserted 10 cm into the ground. Subsequently, the data were corrected by soil temperature and pressure and converted from ppm/s to mol $m^{-2}d^{-1}$ and later to g $m^{-2}d^{-1}$, according to the equation:

$$F = \frac{flux*86400*(P*V)}{10^6*R*T*A}$$

where:

F : CO_2 flux in mol $m^{-2}d^{-1}$
Flux: measurement taken in the field (ppm/s)
P : barometric pressure in mbar
V : the cumulative chamber volume in m^3
R : Gas constant 0.08314510 $barLK^{-1}mol^{-1}$
T : soil temperature in ° K
A : cumulative chamber area in m^2

3.2. GEM (gaseous elemental mercury) measurement method

The GEM concentrations were measured using the Lumex Portable Mercury Vapor Analyzer RA-915+® in monitoring mode (data logger). The route was followed on foot with a GPS device to control the monitoring position. The Lumex Portable Mercury Analyzer RA-915+® is a highsensitivity quantitative analytical device designed for real-time atmospheric Hg measurement. This instrument is a portable multifunctional atomic absorption spectrometer that applies a Zeeman correction for background absorption, which eliminates the effects of interfering impurities. The Hg analysis system pumps air (10 dm^3/min) through an inlet that filters air particles to the detection cell. A zero correction is applied every 20 minutes during the sampling process to restore the baseline by changing the air flow through an Hg absorption filter. The detection limits of this instrument are 0.5-30,000 ng/m^3, and the instrument is accurate to 20% (OhioLumex, 2017).

3.3. ^{222}Rn measurement method

The DURRIDGE RAD 7 Electronic Radon Detector 2684™ was used to measure ^{222}Rn gas. The RAD 7 uses a solid-state alpha radiation detector made out of a semiconductor material (silicon) that converts alpha radiation directly into an electrical signal. This instrument has a soil probe that is placed approximately 50 cm deep into the ground. The measurement mode was set to Sniff in the present study, as the concentrations of ^{222}Rn gas in the soil were high, requiring little time to adjust the accuracy. The measurement method used in the present study was the protocol for thoron (^{220}Rn; Durridge, 2019), in which the equipment takes measurements every five minutes; however, for Rn measurements, the first two readings were ignored to reach equilibrium and obtain an accuracy of ±10%. Thus, readings were taken every five minutes (per quadruplicate) at each sampling point to obtain the concentrations of ^{222}Rn and ^{220}Rn. Subsequently, data management was performed using CAPTURE software (DURRIDGE) to determine the concentrations at each sampling point, corrected by temperature and humidity. Soil temperature was measured at each sampling site using a thermocouple placed 50 cm deep.

3.4. Statistical data management

Common descriptive statistics (mean, median, and standard deviation) were obtained for the data concerning CO_2 flux, GEM concentrations, and soil temperature. Subsequently, statistical data processing was carried out according to the methodology followed by Sinclair (1974) and Lepeltier (1969) for a set of geochemical data. In this methodology, histograms are used to determine whether the data follows a normal distribution. If the data does not follow a normal distribution, a log-normal transformation is performed for the statistical analysis. From this transformation, a cumulative probability diagram is constructed to observe the data behavior, determine whether there are different populations, and establish the background values of the area as well as any possible anomalous values. After the statistical treatment of the data, the background and anomalous values from the first sampling of CO_2 fluxes, soil temperatures, and GEM concentrations were used to construct distribution maps. The statistical management of the data was carried out using Minitab v.19 software. Surfer v.16 software was used with the simple Kriging

interpolation method to construct the distribution maps of CO_2 fluxes and soil temperatures. The minimum curvature interpolation method was used to construct the distribution map of GEM concentrations; this method sought to soften the interpolated surface according to a prespecified parameter.

4. Results

4.1. Statistical distribution of diffuse CO_2 fluxes, GEM concentrations, and soil temperatures

The CO_2 flux, GEM concentration, and soil temperature data were analyzed using the methodology described by Sinclair (1974) and Lepeltier (1969). According to the histograms (Figs. 3A, 4A, and 4B), the dataset shows a distribution different from a normal one. Cumulative probability graphs (Figs. 3A, 4A, and 4B) were constructed using the log-normally (Ln) transformed data to determine the possible existence of several populations within the range of the obtained data and also to determine the background values and possible anomalous values within the study area. All data concerning the Ln transformed CO_2 fluxes (Ln CO_2) followed the same trend on the normal distribution line (Fig. 3B). However, three data points did not follow a normal distribution, and these data points had the highest values; these points were categorized as anomalous values of the population because they represented areas in which there was greater degassing compared to rest of the studied area. The average value (50%) of the CO_2 fluxes that followed the same trend, which made up 95.25% of the total data (Fig. 3B), was used to establish the background value (15.39 g $m^{-2}d^{-1}$). The background value was used as the minimum limit for the flux distribution maps, while the maximum CO_2 flux value of this population (44.12 g $m^{-2}d^{-1}$) was used to determine the normal degassing values (biogenic and/or geogenic) for the study area.

The same calculations were carried out for the GEM concentration dataset (Figs. 4A and 4B) and for the soil temperature data obtained at each CO_2 flux sampling point, which exhibited log-normal behavior in the data transformation process. As with the data concerning CO_2 fluxes, the statistical management of the data concerning GEM concentrations and temperatures was used to determine the background, normal values, and anomalies of the area.

4.2. CO_2 fluxes and soil temperatures

The CO_2 fluxes obtained in the first November campaign ranged from 4.38 to 94.61 g $m^{-2}d^{-1}$ (Table 1). The average CO_2 flux value of the background data population was 15.39 g m^2d^{-1} (Fig. 3B), which was

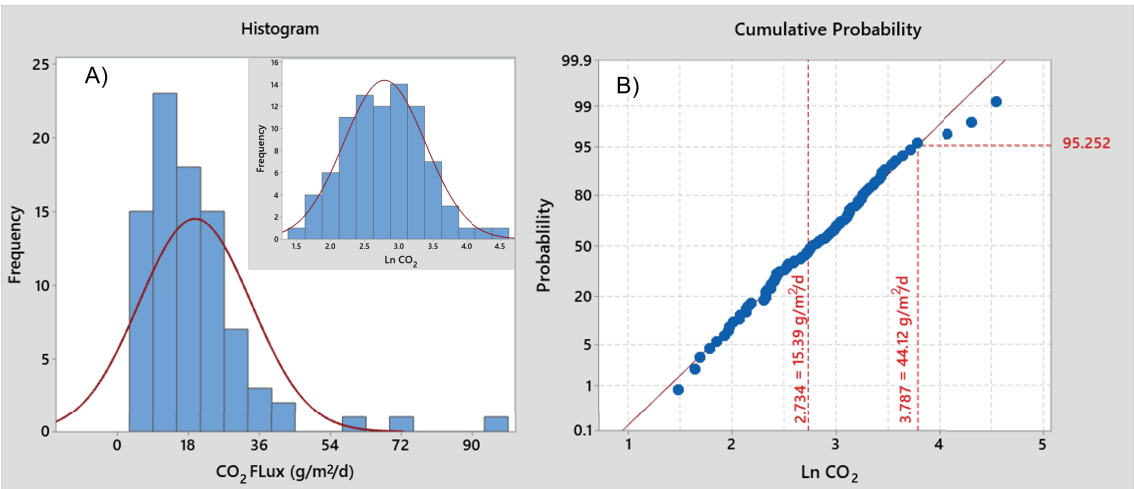

FIG. 3. Histograms and cumulative probability curve the CO_2 flux for samples gathered in November 2018. **A)** The first histogram shows the non-normal distribution behavior of the CO_2 fluxes (g/m²/d) data set, and the second histogram shows the normal distribution behavior of the CO_2 lognormal transformed data set. **B)** The cumulative probability curve shows the normal distribution behavior of LnCO_2 data set, the background population average value (15.39 g/m²/d) and the threshold flux value (44.12 g/m²/d) in the study area according to data statistical treatment (Sinclair, 1974; Lepeltier, 1969).

TABLE 1. BASIC STATISTICIANS OF DIFFUSE GAS VALUES MEASURED IN THE ARARÓ-SIMIRAO GEOTHERMAL SYSTEM, IN THE SAMPLING CAMPAIGNS CARRIED OUT IN DRY (MAY) AND RAINY SEASON (AUGUST AND NOVEMBER).

Variable	Campaign	Data number	Minimum	Maximum	Mean	Median	Std. Dev.
					($g\ m^{-2}d^{-1}$)		
CO_2	November 2018	86	4.38	94.61	19.61	15.98	14.21
	May 2019	38	0.80	1,421.80	65.70	8.20	237.30
					(°C)		
SOIL temperature (samples of CO_2)	November 2018	86	15.80	46.20	26.21	25.40	5.07
	May 2019	38	25.10	71.50	45.28	42.05	12.61
					(ng/m^3)		
Hg	August 2018	8,385	0.50	365.51	3.46	2.07	10.28
	November 2018	18,576	0.49	2,914.46	6.31	3.35	43.28
					(Bq/m^3)		
^{222}Rn	May 2019	6	1,060	124,000	59,905	58,000	58,381
					(°C)		
SOIL temperature (samples of ^{222}Rn)	May 2019	6	32.7	58.1	41.3	39.68	8.88

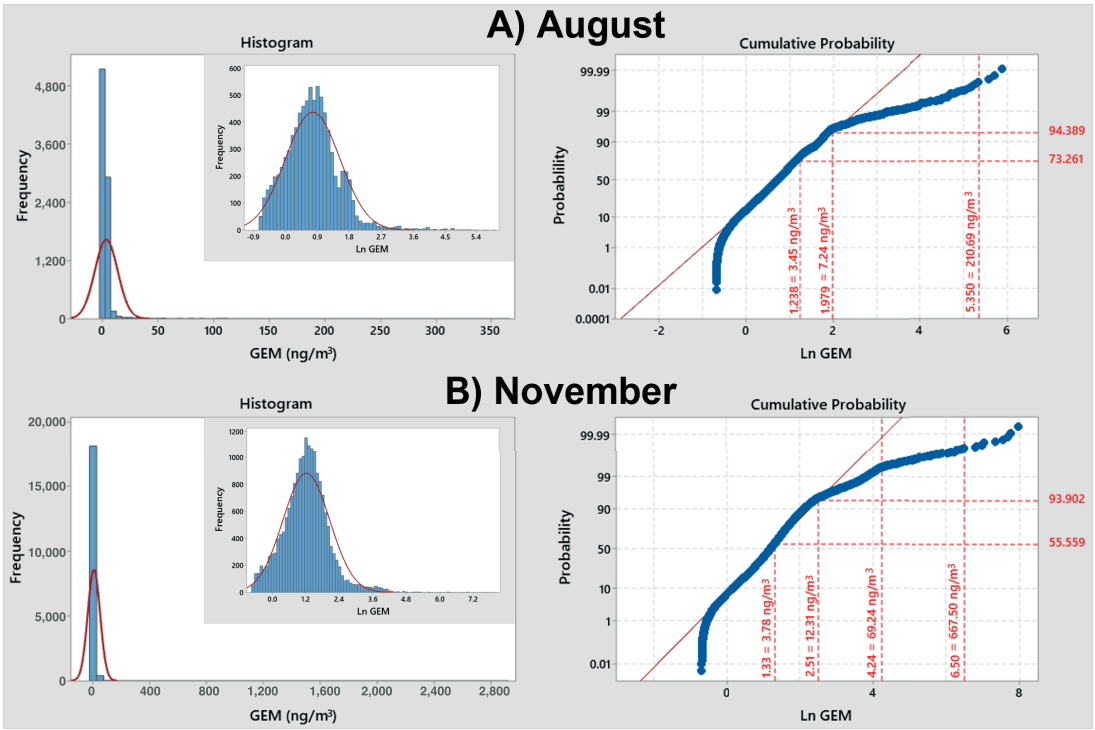

FIG.4. Histograms and cumulative probability curve of the GEM (gaseous elemental mercury) data obtained in August and November 2018. **A)** The histograms shows the non-normal distribution behavior of the GEM data and normal distribution behavior of the transformed data set (Ln GEM) for August sampling campaign. The cumulative probability curve shows the background average (3.45 ng/m^3), threshold (7.24 ng/m^3) and extremes (>210.69 ng/m^3) values for the study zone. **B)** The histograms shows the non-normal distribution behavior of the GEM data and normal distribution behavior of the transformed data set (Ln GEM) for November sampling campaign. The cumulative probability curve shows the background average (3.78 ng/m^3), threshold (12.31 ng/m^3), anomalies zones (69.24 ng/m^3) and extremes (>667.50 ng/m^3) values for the study zone.

relatively close to the average value of the total dataset 19.61 g $m^{-2}d^{-1}$ and comparable to other background values in hydrothermal systems associated with high degassing, magmatic conditions, and nonmagmatic conditions at depth (Harvey *et al.,* 2017). The range of CO_2 fluxes in the study area was similar to that of the reported values of normal soil respiration (several tens of g $m^{-2}d^{-1}$; Chiodini *et al.,* 2008) as well as that of the degassing values of volcanic soils both with and without vegetation (approx. 10^3-10^4 g $m^{-2}d^{-1}$; Chiodini *et al.,* 2008). The statistical analysis showed that the average CO_2 flux value of the background population was 15.39 g $m^{-2}d^{-1}$ and that the threshold value (biogenic and/or geogenic) of the study area was 44.12 g $m^{-2}d^{-1}$. Only values above the threshold value were plotted in the flux distribution map (Fig. 5), and values that exceeded 44.12 g $m^{-2}d^{-1}$ were taken to be anomalous degassing zones. According to figure 5, the highest fluxes (94.61 g $m^{-2}d^{-1}$) were located near the Araró-Simirao fault (mud pool, south of the study area); this was the only area with a higher-than-normal degassing value. This finding suggests that the study area has homogeneous degassing; this can be explained by the type of soil (gleysol) in the area (which forms an impermeable layer), by the lack of highpermeability areas reaching the surface, and/or by groundwater serving as a CO_2 carrier solubilized in the aquifer.

In the second sampling campaign (May), a narrower mesh (approximately 10 m between points) was applied to the anomalous area (mud pool) detected during the November sampling campaign (Zone A). Fluxes of 0.80 to 1,421.80 g $m^{-2}d^{-1}$ (Table 1) were obtained, with an average of 65.70 g $m^{-2}d^{-1}$; these values were higher than those found in the first sampling campaign. This was probably due to the dry season, which corresponds to less humidity in the soil and a deeper aquifer water table, as CO_2 is a gas that dissolves easily in groundwater and can be carried away from the principal upstream areas (Marrero *et al.,* 2008; Clark, 2015). This results in a decrease in soil degassing during the rainy season. The CO_2 distribution map of this area (Fig. 5, Zone A) displays two anomalous points very close to each other (<50 m). The highest fluxes (1,421.8 g $m^{-2}d^{-1}$) were found on the Araró-Simirao fault trace, where it intersects with one of the NNE-SSW lineaments. These values were similar to those reported in other fault-dominated geothermal systems with numerous lineaments (*e.g.,* 1,467.5 g $m^{-2}d^{-1}$ in Brady's system in the Basin and Range Province, Nevada, USA; Jolie *et al.,* 2015). This indicates a point of high permeability, where CO_2 can ascend from a deep area to the surface. It should be noted that these points were very restricted and that the surrounding fluxes had normal values.

The soil temperature in the November sampling ranged between 15.8 and 46.2 °C (Table 1). The annual mean atmospheric temperature (17.4 °C) was taken as the threshold value of the zone. As shown in figure 5, one anomaly was located in the area with the largest CO_2 degassing (mud pool) and the highest soil temperature values (46.2 °C) in the southern part of the study area (Zone A). Another anomalous value was found in the central area at Los Hervideros (temperature=45.5 °C) and Huingo (temperature=36.3 °C) in Zone B. The temperature increase in this zone was likely due to its proximity to superficial thermal manifestations, while the first anomaly could have been associated with a point of greater permeability (normal fault) and high CO_2 degassing.

The anomalous areas (found previously) were sampled in the May campaign. The soil temperatures ranged between 25.1 and 71.5 °C (Table 1), and the highest temperature once again corresponded with the highest CO_2 flux area (mud pool; Fig. 5). This corroborates the anomaly found in the first sampling campaign, albeit at a higher temperature. As shown in figure 5, this area showed a tendency for increased soil temperatures toward the north with respect to the Araró-Simirao fault trace. High soil temperatures were observed (maximum=57.8 °C) in the anomaly at the center of the study area (Zone A, May campaign), corroborating what was found in the first sampling campaign. Figure 5 shows an increase in temperature which was associated with thermal springs, faults and the NNW-SSE lineaments. A similar pattern was also observed toward the western sector in an area where there was evidence of ancient thermal manifestations (sinter), which were probably associated with a NNE-SSW lineament (Zone B, May campaign). CO_2 flux measurements were also taken in this area, but the range of CO_2 flux values fell within the range of background values for the study area. With regard to CO_2 flux, the soil temperature was higher in the second field season sampling campaign; this was probably due to the dry weather conditions, in which differences in humidity and the water table position of the aquifer play important roles as flow and temperature medium moderators.

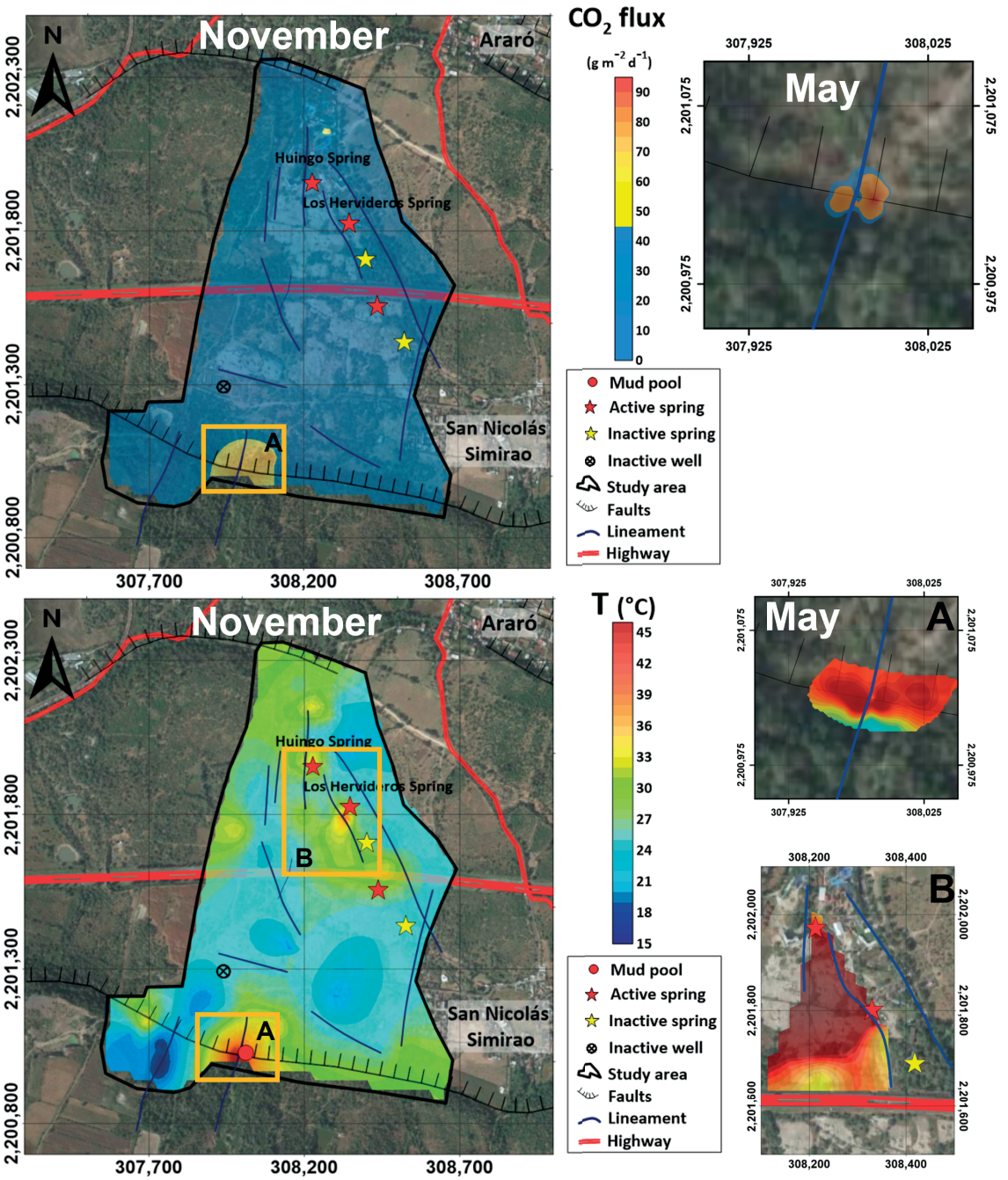

FIG. 5. CO_2 flux (upper panel) and soil temperature (lower panel) distribution maps for the samplings carried out in November 2018 and May 2019. The CO_2 flux distribution map for November 2018, shows an anomaly zone **(A)** with fluxes greater than the threshold value (44.12 g $m^{-2}d^{-1}$) for the study area; in the map only fluxes above threshold value were plotted. The CO_2 flux anomaly zone sampled in May 2019 denominated mud pool, with maximum fluxes of 1,421.80 g $m^{-2}d^{-1}$. The soil temperature distribution map for November 2018, shows two anomalous zones (**A** and **B**) with temperatures greater than threshold temperature of the study area (17.4 °C). The anomaly **A** map (mud pool zone) show the maximum soil temperature (71.8 °C) observed in sampling of May 2019. The anomaly **B** (the thermal active spring area) shows an increase in soil temperature with increasing fracturing, observed in sampling of May 2019.

4.3. GEM concentrations

During the August campaign, the range of GEM concentrations fluctuated between 0.5 and 365.51 ng/m^3 (Table 1). Statistical management of the data concerning GEM concentrations was carried out in the same way as for the data concerning CO_2 fluxes and soil temperatures (Fig. 4). The background population average of the GEM concentrations in the study area was 3.45 ng/m^3; GEM concentration values were considered anomalous if they were above 7.24 ng/m^3 (threshold value) and deemed extreme if they exceeded 210.69 ng/m^3 (Fig. 4A). In this way, two GEM anomalies were detected (Fig. 6). One anomaly with a maximum value of 184.2 ng/m^3 (Fig. 6, Zone B) was detected in the old thermal manifestations of the La Salud balneary near the town of San Nicolás Simirao and a NNW-SSE lineament. Another (higher) anomaly with a GEM concentration of up to 363.56 ng/m^3 (Fig. 6, Zone A) was detected near the Araró-Simirao fault trace (extreme value), which coincided with the area with the highest CO_2 flux (mud pool) and soil temperature. These GEM values were similar to those found in other areas with both volcanic and geothermal activity (Varekamp and Buseck, 1986) oscillating between 35 and 1,031 ng/m^3.

The GEM values obtained in the November campaign ranged between 0.49 and 2,914.46 ng/m^3 (Table 1); the average background value was 3.78 ng/m^3, and the anomalies were considered to be above 12.31 ng/m^3. Two anomalous populations were identified: one with a maximum value of 69.24 ng/m^3, and another with a maximum value of 667.50 ng/m^3. Extreme values were considered to be above the maximum value of the second anomalous population (Fig. 4B). Three anomalous zones were found, confirming the two anomalous zones that were previously detected (Fig. 6). The first anomalous zone had a low GEM concentration of 115.1 ng/m^3 (Fig. 6, Zone C) and was located in the north-central part of the study area, near the active thermal manifestation (Los Hervideros Balneary) and over a NW-SE lineament. The second anomalous zone had a maximum GEM concentration of 200.56 ng/m^3 (Fig. 6, Zone B), was located in the central part of the study area, and corresponded to one of the anomalies found in the first sampling campaign (Fig. 6, Zone B). The third anomaly presented with the highest GEM concentration of 2,914 ng/m^3 (Fig. 6, Zone A) and coincided with the area of the mud pool found in the first sampling campaign. The GEM concentration measured in this last anomalous zone was above the GEM values reported in areas associated with volcanism, such the Colima Volcano (western Mexico) and Hawaii (1,422 and 1,031 ng/m^3, respectively; Voltattorni *et al.,* 2010; Varekamp and Buseck, 1986). According to Varekamp and Buseck (1986) and Murray (1997), these anomalies occur when geothermal fluids ascend from a deep reservoir to shallow levels; thus, the GEM anomalies found in the study area may have been related to the temperatures of ascending geothermal fluids acting as carriers, in the fault or lineaments zones which can act as migration routes for gases (Phuong *et al.,* 2012). In addition, the largest GEM anomaly found in this study suggests a vertical gas migration zone extending from a deep reservoir to the surface.

4.4. ^{222}Rn concentrations

The ^{222}Rn concentrations found in this study ranged between 1,060 and 124,100 Bq/m^3 (Table 1), and the highest concentrations were found nearest to the mud pool (Fig. 7A); moving away from this area, the measured concentrations decreased. This concentration range was greater than those reported in geothermal and volcanic areas, such as the Tetitlan Valley in Nayarit, Mexico (average ^{222}Rn concentration =2,702 Bq/m^3; Voltattorni *et al.,* 2010) and the San Miguel Volcano in El Salvador (average ^{222}Rn concentration=30,821 Bq/m^3; Cartagena *et al.,* 2004). These measurements suggest that high levels of ^{222}Rn degassing occurred over a high-permeability area due to the crossing of the two aforementioned geological structures as well as a deep origin (Jolie *et al.,* 2015; Giammanco *et al.,* 2007; Voltattorni *et al.,* 2010; Israde-Alcántara and Garduño-Monroy, 1999; Viggiano-Guerra and Gutiérrez Negrín, 2003).

On the other hand, ^{220}Rn concentrations ranged from 0 to 7,511 Bq/m^3 (Table 1 and Fig. 7B), indicating high concentrations of this isotope at the points that had lower levels of ^{222}Rn degassing. ^{220}Rn anomalies can be induced by geothermal effects in areas with average gas flow rates and can be related to surface structures or gas origins that are close to the surface. These anomalies are also associated with lacustrine and alluvial deposits, which favor the accumulation of this gas due to its low permeability (Jolie *et al.,* 2015). In the case

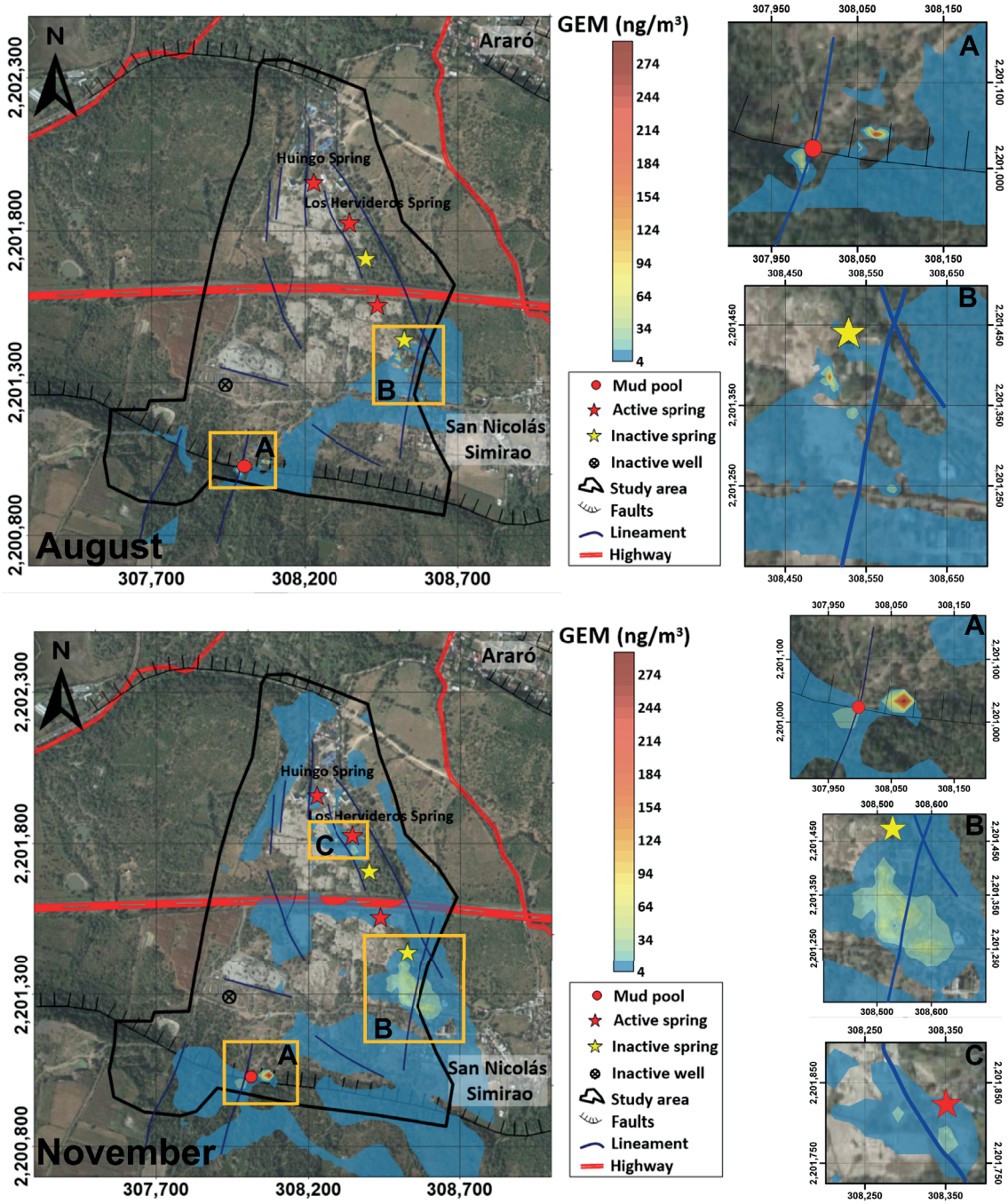

FIG.6. GEM (gaseous elemental mercury) content distribution maps for the samplings carried out in August and November 2018. GEM sampling carried out in August (upper part) shows two anomalies, the mud pool zone **(A)** and east part zone next to San Nicolás Simirao town **(B)**, with GEM values above the threshold value (7.24 ng/m^3) for the study area. GEM content distribution map for sampling carried out in November (lower part) shows three anomalies, the mud pool zone **(A)** and east part zone next to Simirao town **(B)**, corroborating the first sampling, and other zone in the thermal actives springs area **(C)**, with GEM values above the threshold value (12.31 ng/m^3). The GEM values reached a maximum of 2,914. 46 ng/m^3 in the mud pool area.

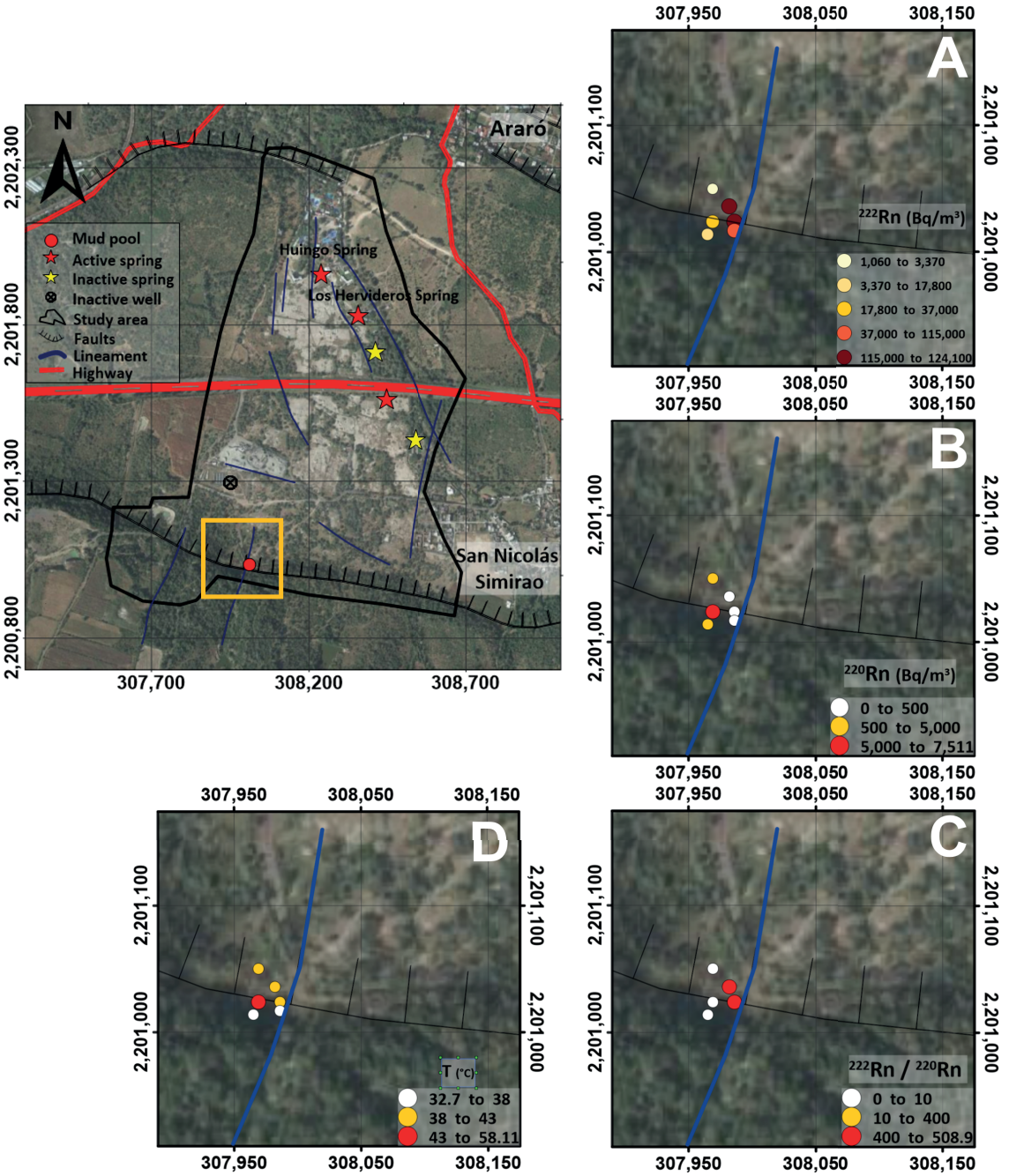

FIG. 7. ^{222}Rn, ^{220}Rn concentration and soil temperature maps in the mud pool zone of the geothermal system, for sampling campaign of May 2019. **A)** ^{222}Rn concentrations with values between 1,060 and 124,100 Bq/m^3. **B)** ^{220}Rn concentrations with values between 0 and 7,511 Bq/m^3. **C)** ^{222}Rn / ^{220}Rn ratios and **D)** soil temperatures in the sampling points of the Rn measurements.

of the sampled area, being near an area with high permeability, the high concentrations are likely due to the geothermal effect.

The $^{222}Rn/^{220}Rn$ ratios ranged from 1 to 508.9 (Fig. 7C). These ratios have been used as indicators to determine areas of high permeability (*e.g.,* faults and fractures), to distinguish between deep (high ratios) and shallow (low ratios) origins in active faults, and to determine the extent of deep faults that connect the deep zone to the surface (Jolie *et al.,* 2015; Phuong *et al.,* 2012). In the case of the sampled area, the $^{222}Rn/^{220}Rn$ ratios were high at points near the mud pool and decreased as they moved away from it (Fig. 7C). These high ratios suggest that the mud pool is a zone of direct, deep degassing of the geothermal reservoir.

The soil temperatures measured at these points ranged between 32.70 and 58.11 °C (Table 1 and Fig. 7D); however, the point with the highest temperature was the point at which the highest concentration of ^{220}Rn was found, assuming that the gas can be transported from a deep source with a high migration rate, which is produced by geothermal effects (*e.g.,* convective processes) in a high-permeability zone.

5. Discussion

5.1 Relationships between diffuse gas emission concentrations in soils and faults zones.

The statistical treatment of the data revealed anomalies directly associated with the Araró-Simirao fault (Fig. 1). The largest anomalies in CO_2 flux, GEM concentration, ^{222}Rn concentration, and soil temperature were observed in the Araró-Simirao fault trace with the crossing of the NNE-SSW lineament, that was related to the zone of the greatest permeability (in the mud pool). Additionally, it was inferred that two of the anomalies in GEM concentration were located in a N30°W secondary fracture zone with argillic alteration and silicification (Ávalos, 2016). This zone was located in the eastern part of the study area, and fracturing was indicated by the lineaments of both ancient and current thermal manifestations. The soil temperature anomalies were spatially similar to the anomalies in GEM concentration, suggesting similar fracturing. Another anomaly was identified toward the central and western part of the study area in a sector of ancient thermal manifestations, which were evidenced by surface sinter deposits.

On the other hand, the CO_2 anomaly was consistent with the highest ^{222}Rn concentrations, GEM concentrations, and soil temperatures. This finding suggests the presence of a gas channels in this area, which would allow CO_2 upward migration to act as a carrier of trace species (in this case, ^{222}Rn and GEM) to the surface (Etiope and Martinelli, 2002; Cartagena *et al.,* 2004; Voltattorni *et al.,* 2010). CO_2 can be considered a carrier gas due to its high concentrations in geothermal systems (Durrance and Gregory, 1987; Mörner and Etiope, 2002). Based on the obtained $^{222}Rn/^{220}Rn$ ratios, these gases can be considered to originate in a deep reservoir and reach the surface through high-permeability migration channels associated with faults and/or fractures (Etiope and Martinelli, 2002; Voltattorni *et al.,* 2010; Phuong *et al.,* 2012; Jolie *et al*., 2015; Bagnato *et al.,* 2018). These migration channels may have occurred in the mud pool area, resulting in a direct ascent from the geothermal reservoir to the surface. The other zones of anomalous GEM concentrations and temperatures are considered to have been caused by existing thermal springs associated with sites of structural weakness, such as the NNW-SSE and NNE-SSW lineaments. These lineaments may correspond to reactivated faults due to the activity of the primary E-W faults, as has been observed to the east of the Graben de Cuitzeo (*e.g.,* Mendoza-Ponce *et al.,* 2018); alternatively, they may correspond to R' or tension (T) fracture-fault systems due to their orientation with respect to the main E-W faults. Thermal discharges in the Araró-Simirao geothermal system are related to zones of high permeability, which are controlled by the main E-W and NE-SW faults and by the NWSE system. Similarly, thermal discharges observed in the Los Azufres geothermal field and the Tizitzio-La Escalera geothermal system, south of Araró-Simirao, are controlled by E-W extensional faults within the TMVB (González-Partida *et al.,* 2000; Jácome-Paz *et al.,* 2019) and reactivated fault systems related to Riedel deformation models (*e.g.,* R', P', N, and T faults with NW-SE and NE-SW orientations; Jácome-Paz *et al.,* 2020).

The relationships between the tectonic structures (faults, fractures, and/or lineaments) that affect the hydrothermal system and the diffuse gas anomalies found in this study were used to develop a conceptual

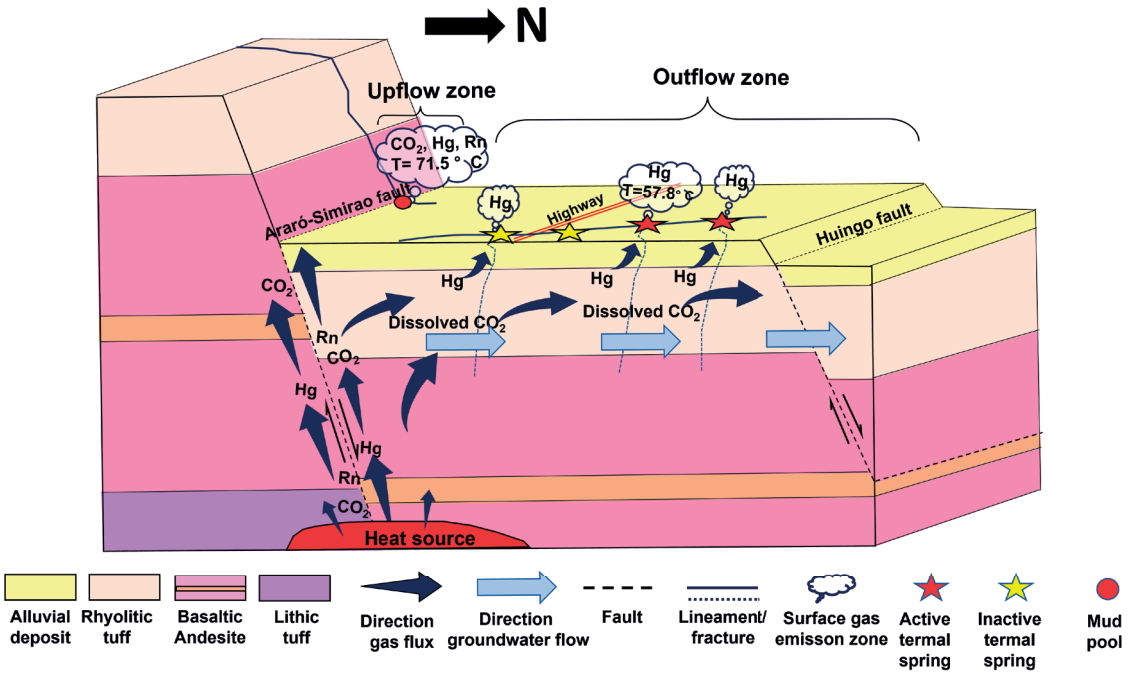

FIG. 8. Conceptual model of the Araró-Simirao geothermal system. The figure shows the upflow zone where the diffuse gases (CO_2, Hg and Rn) are transported from the depth to the surface through an area of greater permeability (Araró-Simirao fault trace), and the outflow zone in the area where the thermal springs and fractures and/or lineaments are located (The depth of the heat source is not to scale).

model of the hydrothermal system (Fig. 8). This model suggests that the area of the mud pool located in the Araró-Simirao fault is the vertical ascent zone of diffuse gases from the deep reservoir (upflow zone) and that the lineaments and/or fractures are areas of structural weakness, in which the GEM gases are associated with the temperatures of the escaping thermal manifestations (outflow zone). Also, the model showed that the low CO_2 content in these areas is most likely due to the high solubility of CO_2 in water, which allows it to be carried by the groundwater flow that runs in the S-N direction toward the Cuitzeo Lake. According to Viggiano-Guerra and Gutiérrez-Negrín (2003), this system resembles a stockwork reservoir, which is associated with fracture zones and located between two deepening faults, exhibiting high vertical permeability in fault zones and low permeability in other areas.

6. Conclusions

The Araró-Simirao geothermal system, located in the southeastern part of the Cuitzeo basin, presents surface manifestations such as thermal springs with temperatures reaching the boiling point (Los Hervideros and Huingo springs) as well as degassing zones through the soil and a mud pool. This area is affected by an E-W normal fault system that forms a halfgraben with dipping blocks northward. The studied area contains two main faults—the Araró-Simirao and Huingo normal faults to the south and north of the area, respectively—as well as associated NNW-SSE and NNE-SSW lineaments or fractures. Based on the diffuse gas emissions (CO_2, GEM, and ^{222}Rn) in the soils of this geothermal system, the following conclusions were reached:

- The Araró-Simirao fault and the NNW-SSE and NNE-SSW lineaments are directly associated with the surface thermal manifestations and diffuse gas anomalies found in the hydrothermal system because these are areas of high permeability.
- The area called the mud pool (located at the intersection of the Araró-Simirao fault trace with a NNE-SSW fracture) with a high degassing rate, represents a vertical upflow zone with ascent of gases from a deep reservoir.
- The NNW-SSE and NNE-SSW lineaments serve as a secondary degassing zone (outflow zone).

- The concentrations of the diffuse gases (CO_2, GEM, and ^{222}Rn) in the studied soils were similar or higher than those reported in other geothermal areas affected by volcanism or large tectonic faults.
- CO_2 may function as a carrier of Hg and ^{222}Rn in the vertical ascent zone (upflow zone). In the outflow zone, CO_2 may be present dissolved in the groundwater. However, it is necessary to perform a more complete sampling of ^{222}Rn to determine its correlation with CO_2.
- It is important to consider sampling temporality, as diffuse gas emissions in soils decrease during the rainy season due to soil saturation, thus reducing the diffusion of gases on the surface.

Acknowledgement

This work was funded by project P02 of the CeMIE-GEO, as well as by internal project-Geophysics Institute, UNAM. We thank the Geothermal Fluid Geochemistry Unit (GFGU) of the Geophysics Institute, Morelia Unit, UNAM for the scientific and analytic support, as well as Ph.D. C. Inguaggiato of the Ensenada Scientific and Higher Education Research Center (CICESE) and Ph.D. V. Yutsis of the Applied Geosciences Division, Potosin Institute of Scientific and Technological Research, (IPICYT) for scientific support, M. López Bastida and B. Ávila Ciprés for field assistance. The authors acknowledgement the anonymous reviewer for his valuable comments.

References

Ávalos, T.D. 2016. Reconocimiento de las asociaciones minerales de alteración y depósitos hidrotermales relacionados con la actividad de los manantiales termales de Araró, Michoacán. Tesis de Licenciatura (Unpublished), Facultad de Ciencias de la Tierra León, Universidad Autónoma de Nuevo León: 89 p.

Bagnato, E.; Parello, F.; Valenza, M.; Caliro, S. 2009. Mercury content and speciation in the Phlegrean Fields volcanic complex: Evidence from hydrothermal system and fumaroles. Journal of Volcanology and Geothermal Research 187: 250-260.

Bagnato, E.; Viveiros, F.; Pacheco, J.E.; D'Agostino, F.; Silva, C.; Zanon, V. 2018. Hg and CO_2 emissions from soil diffuse degassing and fumaroles at Furnas Volcano (São Miguel Island, Azores): Gas flux and thermal energy output. Journal of Geochemical Exploration 190: 39-59. doi: 10.1016/j.gexplo.2018.02.017.

Cabassi, J.; Tassi, F.; Venturi, S.; Calabrese, S.; Capecchiacci, F.; D'Alessandro, W.; Vaselli, O. 2017. A new approach for the measurement of gaseous elemental mercury (GEM) and H_2S in air anthropogenic and natural sources: Examples from Mt. Amiata (Siena, Central Italy) and Solfatara Crater (Campi Flegrei, Southern Italy). Journal of Geochemical Exploration 175: 48-58.

Cartagena, F.; Olmos, R.; López, D.L.; Soriano, T.; Barahona, F.; Hernández, P.A.; Pérez, N.M. 2004. Diffuse soil degassing of carbon dioxide, radon, and mercury at San Miguel volcano, El Salvador. *In* Natural Hazards in El Salvador. Geological Society of America. Special Paper 375: 203-212. doi: 10.1130/0-8137-2375-2.203.

Chiodini, G.; Caliro, S.; CArdellini, C.; Avino, R.; Granieri, D.; Schmidt, A. 2008. Carbon isotopic composition of soil CO_2 efflux, a powerful method to discriminate different sources feeding soil CO_2 degassing in volcanic-hydrothermal areas. Earth and Planetary Science Letters 274: 372-379.

Clark, I. 2015. Groundwater geochemistry and isotopes. Taylor and Francis Group. New York: 442 p.

CONAGUA. 2018. Actualización de la disponibilidad media anual de agua en el acuífero Morelia-Queréndaro (1602), Estado de Michoacán. Comisión Nacional del Agua. Gerencia de Aguas Subterráneas: 34 p.

DETENAL (Dirección General de Estudios del Territorio Nacional) 1978. Carta Geológica Zinapécuaro E14A14, Escala 1:50.000.

Durrance, E.M.; Gregory, R. G. 1987. Helium and radon transport mechanisms, heat flow and hydrothermall circulation in SW England. *In* Proceedings of the Ussher Society 6 (4): 555- 556.

Durridge. 2019. RAD 7 Electronic Radon Detector, User manual. Durridge Radon Capture and Analytics: 94 p.

Etiope, G.; Martinelli, G. 2002. Migration of carrier and trace gases in the geosphere: An overview. Physics of Earth Planetary Interiors 129: 185-204. doi: 10.1016/S0031-9201(01)00292-8.

Ferrari, L.; Orozco-Esquivel, T.; Manea, V.; Manea, M. 2012. The dynamic history of the Trans-Mexican Volcanic Belt and the Mexico subduction zone. Tectonophysics. 522-523: 122-149. doi: 10.1016/j.tecto.2011.09.018.

Fridriksson, T. 2009. Diffuse CO_2 degassing through soil and geothermal exploration. Short Course on Surface Exploration for Geothermal Resources. *In* United Nations University-Geothermal Training Programme and LaGeo: 1-6 p. El Salvador.

Garduño-Monroy, V.H. 2019. Estudio de fracturamiento-fallamiento y campo de deformación actual y modelos

numéricos apoyados con sísmica y geofísica de exploración en los campos geotérmicos de Cuitzeo, Michoacán, Rancho Nuevo, Guanajuato, Las Derrumbadas, Puebla, y Volcán Tacaná. http://cemiegeo.org/index.php/proyectos/desarrollo-e-innovacion-de-tecnicas-de-exploracion/p17/9-linea-de-investigacion/proyecto/23-p17. (Last visit: 01/10/2020).

Garduño-Monroy, V.H.; Israde-Alcántara, I.; Francalanci, L.; Carranza, O.; Chiesa, S.; Corona, P.; Arreygue, E. 1997. Sedimentology, volcanism, and tectonic southern margin of the lacustrine basins of Maravatio and Cuitzeo, Michoacan, Mexico. IAVCEI, General Assembly: 24 p. Puerto Vallarta.

Garduño-Monroy, V.H.; Pérez-López, R.; Israde-Alcantara, I.; Rodríguez-Pascual, M.A.; Szynkaruk, E.; Hernández-Madrigal, V.M.; García-Zepeda, M.L.; Corona-Chávez, P.; Ostroumov, M.; Medina-Vega, V.H.; García-Estrada, G.; Carranza, O.; López-Granados, E.; Mora-Chaparro, J.C. 2009. Paleoseismology of the southwestern Morelia-Acambay fault system, central Mexico. Geofísica Internacional 48 (3): 319-335.

Giammanco, S.; Sims, K.W.; Neri, M. 2007. Measurements of ^{220}Rn and ^{222}Rn and CO_2 emissions in soil and fumarole gases on Mt. Etna volcano (Italy): implications for gas transport and shallow ground fracture. Geochemistry, Geophysics, Geosystems. 8 (10): 1-14. doi: 10.1029/2007GC001644.

Gómez-Tuena, A.; Mori, L.; Straub, S.M. 2018. Geochemical and petrological insights into the tectonic origin of the Transmexican Volcanic Belt. Earth-Science Reviews. 183: 153-181. doi: 10.1016/j.earscirev.2016.12.006.

Gómez-Tuena, A.; Orozco-Esquivel, M.T.; Ferrari, L. 2005. Petrogénesis ígnea de la Faja Volcánica Transmexicana. Boletín de la Sociedad Geológica Mexicana. LVII (3): 227-283. https://dx.doi.org/10.18268/bsgm2005v57n3a2.

González-Partida, E.; Birkle, P.; Torres-Alvarado, I.S. 2000. Evolution of the hydrothermal system at Los Azufres, Mexico, based on petrologic, fluid inclusion and isotopic data. Journal of Volcanology and Geothermal Research, 104 (1-4): 277-296. doi: 10.1016/S0377-0273(00)00211-0.

Gutiérrez-Negrín, L.C.; López-Hernández, A.; Quijano-León, J.L. 1989. Zonas geotérmicas de interés en México. Geotermia. Revista Mexicana de Geoenergía 5 (3): 283-346.

Harvey, M.C.; Rowland, J.V.; Chiodini, G.; Rissmann, C.F.; Bloomberg, S.; Fridriksson, T.; Oladottir, A.A. 2017. CO_2 flux geothermometer for geothermal exploration. Geochimica et Cosmochimica Acta 213: 1-16. doi: 10.1016/j.gca.2017.06.025.

Hernández, J.B.; Landaverde, B.M.; Chávez-Molina, L.M. 2015. Caracterización e interpretación de estructuras geológicas y fumarolas a través de las emanaciones difusas en un área geotérmica de alta entalpía. Programa Regional de Entrenamiento geotérmico (PREG), Diplomado de Especialización en Geotermia-2015. Repositorio Institucional de la Universidad del Salvador.

INEGI. 2009. Prontuario de información geográfica municipal de los Estados Unidos Mexicanos, Zinapécuaro, Michoacán de Ocampo. Instituto Nacional de Estadística y Geografía: 9 p.

Israde-Alcántara, I.; Garduño-Monroy, V.H. 1999. Lacustrine record in a volcanic intra-arc setting: The evolution of the Late Neogene Cuitzeo basin system (central-western Mexico, Michoacan). Palaeogeography Palaeoclimatology Palaeoecology 153 (1-3): 209-227. doi: 10.1016/S0031-0182(99)00024-3.

Jácome-Paz, M.P.; González-Romo, I.A.; Prol-Ledesma, R.M.; Vera, M.T.; Pérez-Zárate, D.; Rodríguez-Díaz, A.A.; Estrada-Murillo, A.M. 2020. Multivariate analysis of CO_2, H_2S and CH_4 diffuse degassing and correlation with fault systems in Agua Caliente-Tzitzio, Michoacán, México. Journal of Volcanology and Geothermal Research 394: 106808. doi: 10.1016/j.jvolgeores.2020.106808.

Jácome-Paz, M.P.; Pérez-Zárate, D.; Prol-Ledesma, R.M.; Rodríguez-Díaz, A.A; Estrada-Murillo, A.M.; González-Romo, I.; Magaña-Torres, E. 2019. Two new geothermal prospects in the Mexican Volcanic Belt: La Escalera and Agua Caliente-Tzitzio geothermal springs, Michoacán, México. Geothermics 8: 44-55. doi: 10.1016/j.geothermics.2019.02.004.

Jennejohn, D. 2009. Research and Development in geothermal exploration and drilling. Geothermal Energy Association, December 2009, 209 Pennsylvania Avenue SE, Washington D.C. 2003. https://geothermalcommunities.eu/assets/elearning/2.16.geo_rd_1209.pdf. (Last visit: 01/10/2020).

Jolie, E.; Klinkmueller, M.; Moeck, I. 2015. Diffuse surface emanations as indicator of structural permeability in fault-controlled geothermal systems. Journal of Volcanology and Geothermal Resources 290: 97-113. doi: 10.1016/j.jvolgeores.2014.11.003.

Lepeltier, C. 1969. A simplified statistical treatment of geochemical data by graphical representation. Economic Geology. 64: 538-550. doi: 10.2113/gsecongeo.64.5.538.

Marrero, R.; López, D.L.; Hernández, P.A.; Pérez, N.M. 2008. Carbon dioxide discharged through the Las Cañadas Aquifer, Tenerife, Canary Islands. *In* Terrestrial Fluids, Earthquakes and Volcanoes: The Hiroshi

Wakita Volume III (Pérez, N.M.; Gurrieri, S.; King, C.; Taran, Y.; editors). Birkhäuser Basel: 147-172.

Mazot, A.; Rouwet, D.; Taran, Y.; Inguaggiato, S.; Varley, N. 2011. CO_2 and He degassing at El Chichón volcano, Chiapas, Mexico: gas flux, origin and relationship with local and regional tectonics. *In* Geochemistry of volcanic fluids: a special issue in honor of Yuri A. Taran (Inguaggiato, S.; Shinohara, H.; Fischer, T.; editors). Bulletin of Volcanology 73 (4): 423-442.

Mendoza-Ponce, A.; Figueroa-Soto, A.; Soria-Caballero, D.; Garduño-Monroy, V.H. 2018. Active faults sources for the Pátzcuaro-Acambay fault system (Mexico): fractal analysis of slip rates and magnitudes Mw estimated from fault length. Natural Hazards and Earth System Sciences 18 (11): 3121-3135. doi: 10.5194/nhess-18-3121-2018.

Mörner, N.A.; Etiope, G. 2002. Carbon degassing from the lithosphere. Global Planetary Change 33 (1-2): 185-203. doi: 10.1016/S0921-8181(02)00070-X.

Murray, K.S. 1997. The use of soil Hg to delineate zones of upwelling in low-to-moderate temperature geothermal systems. Geothermics 26 (2): 193-202.

OhioLumex. 2017. Portable Zeeman Mercury Analyzer Light 915. (n.d.). Disponible en: http://ohiolumex.com/sites/default/files/product_image/Light%20915%20Brochure.pdf (Last visit 21 Sep. 2017).

Owens, L.B. 2013. Geochemical investigation of hydrothermal and volcanic systems in Iceland, New Mexico and Antarctica. Dissertation for Doctor of Philosophy in Earth and Environmental Science (Geochemistry) (Unpublished), New Mexico Institute of Mining and Technology, Department of Earth and Environmental Science, Socorro: 313 p.

Padrón, E.; López, D.; Magaña, M.I.; Marrero, R.; Pérez, N.M. 2003. Diffuse degassing and relation to structural flow paths at Ahuachapán Geothermal Field, El Salvador. Geothermal Resources Council Transactions 27: 325-330.

Peiffer, L.; Carrasco-Núñez, G.; Mazot, A.; Villanueva-Estrada, R.E.; Inguaggiato, C.; Bernard-Romero, R.; Rocha Miller, R.; Hernández Rojas, J. 2018. Soil degassing at the Los Humeros geothermal field (Mexico). Journal of Volcanology and Geothermal Research 356: 163-174. doi: 10.1016/j.jvolgeores.2018.03.001.

Phuong, N.K.; Harijoko, A.; Itoi, R.; Unoki, Y. 2012. Water geochemistry and soil gas survey at Ungaran geothermal field, central Java, Indonesia. Journal of Volcanology and Geothermal Resources 229-330: 23-33. doi: 10.1016/j.jvolgeores.2012.04.004.

Sinclair, A.J. 1974. Selection of threshold values in geochemical data using probability graphs. Journal of Geochemical Exploration 3 (2): 129-149. doi: 10.1016/0375-6742(74)90030-2.

Van Kooten, G.K. 1987. Geothermal exploration using surface mercury geochemistry. Journal of Volcanology and Geothermal Resources 31 (3-4): 269-280. doi: 10.1016/0377-0273(87)90071-0.

Varekamp, J.C.; Buseck, P.R. 1983. Hg anomalies in soils: a geochemical exploration method for geothermal areas. Geothermics 12: 29-47.

Varekamp, J.C.; Buseck, P.R. 1986. Global mercury flux from volcanic and geothermal sources. Applied Geochemistry 1 (1): 65-73. doi: 10.1016/0883-2927(86)90038-7.

Viggiano-Guerra, J.C.; Gutiérrez-Negrín, L.C.A. 2003. Régimen de flujo hidrotermal en la zona geotérmica de Araró, Michoacán, México. Ingeniería Hidráulica en México XVIII (1): 39-53.

Viggiano-Guerra, J.C.; Gutiérrez-Negrín, L.C.A. 2005. The geothermal system ofAraró, Mexico, as an independent system of Los Azufres. Proceedings World Geothermal Congress: 7 p. Antaya.

Vigil, A.J. 2017. Caracterización geológica y geoquímica de fluidos en el sistema geotérmico Araró, Michoacán, México. Tesis de licenciatura (Unpublished). Facultad de Ciencias de la Tierra. Universidad Autónoma de Nuevo León: 105 p.

Voltattorni, N.; Sciarra, A.; Quatrocchi, F. 2010. The application of soil-gas technique to geothermal exploration: Study of hidden potential geothermal systems. Proceedings World Geothermal Congress: 7 p. Bali.

West System. 2019. Portable diffuse flux meter, Handbook. Release 9.1 West System: 104 p.

Manuscript received: February 9, 2020; revised/accepted: November 11, 2020; available online: May 31, 2021.